Aerodynamic effectiveness of the flow of exhaust gases in a generic formula one car configuration

F. L. Parra and K. Kontis
University of Manchester
School of MACE
Manchester, UK

ABSTRACT

The effects of the flow of exhaust gases intentionally orientated on the rear wing element of a generic Formula One car body have been studied. A qualitative analysis of the effectiveness of a cold nitrogen jet on a NACA 0012 type of aerofoil has been conducted. The Reynolds number of the jet was 13,000, based on the jet velocity and diameter, and of the bodywork was 54,000, based on the free stream velocity and bodywork length. The lift coefficient was measured via a three-component strain-gauge force balance at four different ground-to-aerofoil heights (32, 45, 60 and 90mm) and incidence range –20 to +20 degrees. The surface flow patterns were visualised using the oil flow technique and were compared with numerical simulations. Pressure measurements were conducted using pressure tappings. The CFD solver was FLUENT. The RNG k-ε model was selected to solve the turbulent flow transport equations. The numerical study also comprised the investigation of the aspiration generated by exhaust gases when these are ejected inside a duct of greater diameter. A parametric investigation relating the relative diameter of exhaust pipe and outer duct and the relative overlap between the sides of the duct and the exhaust pipe was performed.

NOMENCLATURE

A wetted area or area of heat exchange
B blockage factor
C_L lift coefficient
c chord of aerofoil
d diameter
G generation rate of turbulent kinetic energy
h convection heat transfer coefficient
k turbulent kinetic energy
L lift force
Nu Nusselt number
P pressure
Pr Prandtl number $\quad Pr = c_p\mu/k$
Re Reynolds number $\quad \text{Re} = \rho Ux = \mu$
s span
S strain rate
t thickness
T temperature
U instantaneous velocity
u streamwise velocity fluctuations

Greek symbols

α incidence angle
α_s swirl constant
ε turbulence dissipation rate
μ molecular viscosity
μ_t eddy viscosity
μ_{to} eddy viscosity calculated without swirl
ρ density
Ω characteristic swirl number calculated within FLUENT

Subscripts

a aerofoil
b bodywork
eff effective
i tensor notation
k due to mean velocity gradients
ε based on dissipation
∞ free stream

1.0 INTRODUCTION

Formula One is renowned for being the most technologically demanding branch of motor-sports. In recent years, when the driver input is becoming less important, teams are focusing their efforts in extracting the best from their machinery. In this sense, the aerodynamic efficiency of the car has always been one of the top priorities, and it is not unusual to see a variety of aerodynamic devices designed to increase the down force (negative lift) acting on the car with a minimal increase in drag (wetted area). The velocity of the exhaust gases as they exit the exhaust pipe can reach values of about 240km/h due to the high engine turning speeds and capacity, and exhaust gas temperatures. Therefore, an increment in the down force acting on the car could be obtained if the exhaust jet is aimed at the lower surface of the rear wing element of the racing car.

The motor-sport governing body (FIA) has imposed a new set of regulations effective from 2006 season. Among these new rules, the most remarkable change will take place in the power plant department. The engine capacity will reduce from 3 litres to 2·4 litres and its typical 'V' configuration will change from 10 cylinders to 8 cylinders. Compared with the old engines, these new units will show detrimental effects in terms of the momentum of the exhaust jet, due to the smaller capacity, and increased fluctuations of the flow, due to the smaller number of cylinders. Nevertheless, the new V8 units have been able to consistently run at engine speeds in excess of 20,000rpm, as opposed to 18,000rpm achieved with the old V10 engines, which should contribute to the compensation of exhaust mass flow rate. In addition to the higher engine speeds, the streamwise dimension of the end plates of the rear wing elements has been increased considerably, probably in order to reduce the free expansion of the exhaust gases and, consequently maintain the exhaust jet momentum to enhance down force and to reduce drag or, in other words, acting as a diffuser for the rear wing elements.

One aspect that is also significantly accountable is the almost continuous and fast changing engine regimes, which directly affects the exhaust mass flow rate and, hence, the momentum of the jet. In spite of the fact that race drivers aim to maintain the turning speed of the engine within the spectrum of maximum torque and power, this still implies regime fluctuations of the order of 5,000 to 6,500rpm around most corners. Consequently, the entire range of relative flow conditions must be taken into account in order to decide the angle at which the exhaust pipe should be placed with respect to the ground. Although this is purely part of the individual and specific design process, one can intuitively foresee that, in order to increase the downforce of the wing element, the air mass flow beneath the aerofoil must be increased and, as a result, the ratio of exhaust jet to free stream momentums must be such that under any given engine regime and free stream velocity, the exhaust

jet is deflected towards the underside of the aerofoil. This can be done by setting the exhaust mass flow rate to the maximum obtainable from the engine and the free stream to the minimum value at which aerodynamic grip is comparable to mechanical grip for a specific setup. Whereas aerodynamic grip is generated by the increment in apparent weight of the race car due to the downforce caused by the wing elements, mechanical grip refers to the friction coefficient between the surfaces of the tyres and the tarmac. On the other hand, those problems were overcome during the 2003 and 2004 seasons, when most teams opted for an exhaust configuration that expelled the gases horizontally, ensuring that the flow did not interfere with the windward side of the aerofoils. The temperature of the exhaust gases flowing around the bodywork and close to load carrying elements, such as the rear tyres, the supporting frame of the rear wing and the rear suspension linkage, is often in excess of 1,300K. For bodywork and suspension bars, teams have often selected carbon and ceramic composites, which are capable of sustaining high temperatures whilst conserving their structural properties. In the case of the rear tyres, the extended end plates of the rear wing elements shield most of the heat, thus preventing tyre failures. Nevertheless, there are mechanical parts that can only be manufactured of non heat-resistant materials, such as the suspension dampers, bushes and seals, which are made of rubber or metal alloys. In that sense, cracked or broken exhaust pipes have caused several race retirements in the last few years due to the overheating and consequent failure of such components.

According to Newton's law of cooling, the heat transferred per unit time is proportional to the surface area through which the heat is exchanged[1], as shown in Equation (1). Furthermore, the heat transfer coefficient of a flat plate in cross flow is given by the Nusselt number, Equation (2). Such a configuration is geometrically very similar to that employed in automotive heat exchangers. In most cases, the cold fluid employed is atmospheric air, and in the case of an automotive radiator, this is achieved by placing the device in the free stream, thus becoming one significant source of drag force. Nevertheless, by increasing the airflow through the radiator, for example by increasing the pressure drop between the two sides of the device, the same rate of heat exchange could be achieved with a smaller area.

$$q = hA(T_w - T_\infty) \qquad \ldots (1)$$

$$Nu = 0\cdot332 Pr^{\frac{1}{3}} Re^{\frac{1}{2}} \qquad \ldots (2)$$

Due to the characteristic configuration of a Formula One car, the exhaust pipes pass through the chamber located directly behind the radiators. This chamber is normally shaped so that it enhances the outflow of gases. However, an extra outflow could be generated by inserting the exhaust pipe into a bigger diameter duct to create a mixing stream. Such mixing is believed to generate an aspiration along the outer duct, based on the same principles of operation as an ejector pump. Because this enveloping duct connects the chamber behind the radiator with the atmosphere, an outflow of gases through this passage would increase the efficiency of the radiator. The mixing between the exhaust flow and the air in the chamber behind the radiator must be maximised. A number of studies on the optimisation of the mixing of turbulent jets by introduction of swirl generators have been performed by Mi and Nathan[2], Rahai and Wong[3], Hilgers and Boersma[4] and Rahai et al[5]. The computational study of Reynier and Minh[6] using a 2-equation k-ε model showed that for a high velocity ratio, recirculation from the outer flow towards the centre line of the jet occurs. Riffat et al[7] and Huang et al[8] showed that the performance of an ejector depends strongly on the distance from the nozzle to the inlet of the mixing duct and the shape of the nozzle itself.

In terms of the exhaust jet behaviour with respect to the free stream, the problem has been approached from the Jet-In-Cross-Flow (JICF) viewpoint. The phenomena related to JICF, referred to

as coherent structures, have been investigated for several decades, and extensively summarised by Margason[9]. Hussain[10] tried to define such coherent structures as a 'connected, large scale fluid mass with a phase correlated vorticity over its spatial extend'. Although this is arguably an incomplete definition, it is able to explain several non-linear effects in the JICF concept. In general, coherent structures can be classified in four different types: counter-rotating vortex pair, jet shear layer vortex, wake vortices and horseshoe vortices. The first one in this group is the most dominant of all, and the rest are known as secondary structures, although their effect cannot be neglected. In fact, Rivero *et al*[11] conducted experiments of JIFC in which the genesis of the dominant counter rotating vortex pair is shown to have a strong dependence on the high pressure gradients that develop in the region near the jet. They found that a handle-like structure links the boundary-layer vorticity with the counter rotating pair through upright tornado-like vortices. This result was also seen computationally by Rudman[12], when he simulated a 3-dimensional axisymmetric JICF and found that the boundary-layer fluid is lifted from the boundary layer towards the counter rotating vortices. Nevertheless, the complexity of the flow in the leeward side of the JICF implies that these vortex structures are very difficult to capture when k-ε turbulence model is employed in the simulations[13]. Some of the pioneering and most extensive investigation of JICF was performed by Fric and Roshko[14]. They investigated jets issuing transversely into a cross flow with velocity ratios ranging between 2 and 10, and cross flow Reynolds number of 11,400. They concluded that the flow around a transverse jet does not separate from the jet and does not shed vorticity into the wake. Instead, the wake vortices originate from the boundary layer of the wall from which the jet is issued. It is argued that the closed flow around the jet causes an adverse pressure gradient in the leeward side of the jet. Andreopoulos and Rodi[15] made a comprehensive experimental study of the deflection caused by cross flow on a transverse jet. They found that at small velocity ratios (U_{jet}/U_{stream} 0·5), the jet is bent over abruptly by the cross flow, whereas at higher velocity ratios, the bending over takes place more gradually as the jet penetrates further into the main stream. Reciprocally, the cross flow is deflected around the jet and, at low velocity ratios, lifted over the bent jet. They also found that at low velocity ratios, the cross flow exerts a strong influence over the jet, causing a strongly non-uniform exit velocity profile and a sharp bending over of the jet, which starts already inside the discharge pipe. Other experimental and computational work has been completed by Gogineni *et al*[16] and Morton and Ibbetson[17] with results that support those presented in the present article. Kontis and Stollery[18] have developed a methodology for the analysis of jet-related effectiveness problems. A similar technique has been adopted in the present work for the presentation and analysis of the results.

The present study aims to investigate: a) the improvement of the aerodynamic efficiency of the radiator and, b) the expulsion of the exhaust gases towards the lower surface of the rear wing element of the car.

2.0 EXPERIMENTAL EQUIPMENT AND PROCEDURE

All the experiments were performed in a continuous blow-down open-circuit type wind tunnel with a square cross section. The test section had dimensions 810 × 455 × 455mm (length × height × width). The blockage ratio depended on the incidence of the aerofoil, see Equation (3). It ranged between 7%, at 0° incidence, and 14·6%, at 20° incidence. The free stream was set to 25ms⁻¹.

$$B = \frac{A_{mod}}{A_{wind\_tunnel}} = \frac{t_b \cdot s + s\left(t_a + c \cdot \mathrm{Sin}\,\alpha\right)}{0 \cdot 455^2} \qquad \ldots (3)$$

A composite wood bodywork model and an aluminium NACA 0012 type aerofoil were employed. The profile of the bodywork model was based on the shape of the upper surface of the radiator

pods in a generic modern Formula One car and it was parametrically scaled with no variations in the spanwise direction. The chord of the aerofoil was defined as one third of the chord of the bodywork profile, which is a reasonable approximation of a real Formula One configuration if the total chord of the multi-element rear wing employed in practice is taken into account, see Ref. 19. A side view of the experimental configurations tested is shown in Figure 1. The distance between the exit of the exhaust pipe and the aerofoil pivot point was set to be equal to the chord of the aerofoil (100mm). An arbitrary exhaust exit angle was employed (40° with respect to the horizontal line), and although this might differ somewhat from those seen in practice, the results presented in the paper are applicable.

The presence of the side walls and the roof of the wind tunnel can affect the results and the behaviour of the flow around the model, mainly due to their boundary layer. In order to reduce any induced errors, the diameter of the exhaust pipe was about 55 times smaller than the width of the tunnel. The presence of the exhaust jet caused additional blockage in the wind tunnel, however its extent was difficult to evaluate empirically. Given the relative dimensions of the model and the wind tunnel, and based on the oil flow results, the disturbances caused by the walls in the exhaust region were considered to have negligible effects on the behaviour of the exhaust jet. Certainly, a future CFD study will address those problems in detail and investigate any induced errors.

The experiments were performed at four different ground-to-aerofoil heights, i.e. 32, 45, 60 and 90mm and incidence range -20 to 20 degrees, Fig. 1. Pressurised nitrogen gas (N_2) was employed to simulate the exhaust discharge at 22ms⁻¹, which implied a velocity ratio ($U_{free\ stream}/U_{exhaust}$) of 1·124. This velocity ratio was defined to match that derived from the boundary conditions in the computational study, see section 'Numerical simulation'. The car body was 300mm long and was bolted onto the ground of the wind tunnel, whereas the aerofoil was supported by its pivot point located at ¼ chord length to the three-component force balance via a steel rod. The Reynolds number for the jet was 13,000, based on the jet velocity and diameter, and for the bodywork it was 54,000, based on the free stream velocity and bodywork length.

The three-component balance was clamped on railings, which allowed vertical displacement, on one side of the wind tunnel. In order to calibrate the vertical positioning for the different cases, a ruler was mounted by the side of the balance. The balance incorporated an angular scale, which enabled the accurate modification of the aerofoil incidence. An angular clamp locked the wing element into the required position during the tests. A full description of this device and its operation can be found in Ref. 20.

Initially, the lift coefficient was measured with only the aerofoil inside the test section for the four different heights and range of incidence. The same procedure was repeated with the car body also inside the test section in order to measure the influence of the presence of the model car body on the performance of the aerofoil. Those cases were tested with no exhaust discharge. Once that part was completed, the exhaust flow was enabled, setting the discharge coefficient in terms of velocity ratio between the exhaust and the free stream.

Pressure tappings were employed to monitor the effect of the flow of exhaust gas on the bodywork. A total of 49 pressure tappings were machined on the car body model and were numbered clock-wise, starting with the inner circumference (20mm diameter). The first numbered tapping of every circumference corresponded to the intersection of the circumference with the radial line parallel to the free stream flow and downstream of the exhaust exit. Figure 2 depicts an enlarged view of the location and numbering of the pressure tappings near the exhaust exit. The precise Cartesian co-ordinates of the 49 tappings are displayed in Table I. These have been deduced assuming the axial origin (0,0) at the centre of the exhaust jet and with the positive direction of the *x*-axis and *y*-axis as depicted in Fig. 2, where the shaded area represents the location of the exhaust pipe. The distances are expressed in millimetres.
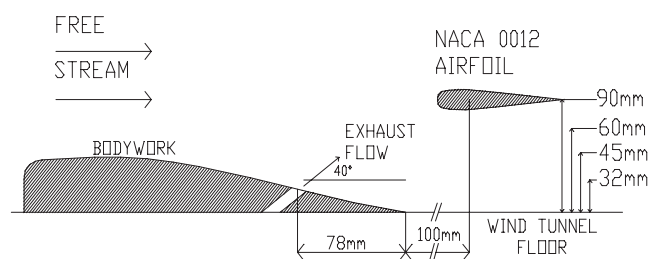
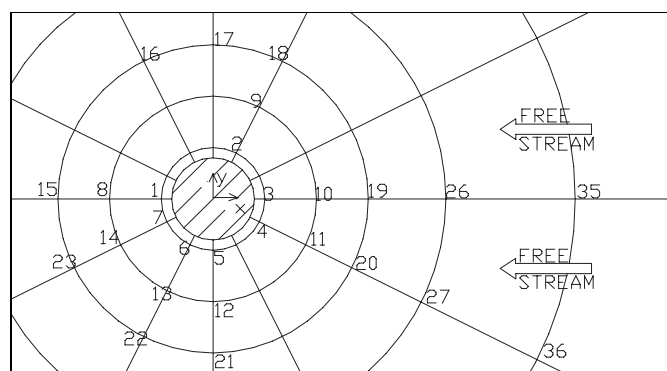Figure 1. Side view of experimental configuration.

Figure 2. Location and numbering of pressure tappings on the bodywork.

The accuracy of the pressure measurements was ±1·5%. The accuracy of the lift coefficient measurements was ±2%.

Initially, the flow around the aerofoil and the car body was visualised using the oil flow technique. The oil flow mixture consisted of titanium oxide and paraffin oil[21]. Pictures were taken with a Canon digital camera placed against the wind tunnel window to avoid reflections.

3.0 NUMERICAL SIMULATION

The main objective of the numerical simulation studies was to study the induced flow caused by the negative pressure gradient generated when the engine gases are exhausted inside a duct of greater diameter than that of the exhaust pipe, Fig. 3. That study was aimed to find a relationship between the relative diameter of the exhaust pipe and the outer duct and the amount of overlap between them.

The nature of that investigation, in which a design evaluation of the exhaust configuration must be made, hinted rapidly the potential benefits of following a computational approach. In addition, the comparatively reduced dimensions of the passage through which the flow is induced makes the experimental measurement of flow velocity in that area extremely difficult; taking into consideration the

limited size of the wind-tunnel facilities and, consequently, the need to scale down the model.

The mathematical code employed was FLUENT. Hybrid meshing scheme was employed, with structured grid in the majority of the flow domain, except for the exhaust and radiator areas, where unstructured mesh was employed. In cases of complex geometry, unstructured grids are advisable, as they adapt to solid boundaries better than structured quadrilateral/hexahedral grids. Nevertheless, care must be taken when constructing the grid, as sharp corners can make the centroid of the cell lay outside the cell itself, causing instabilities in the solver. In order to avoid these sort of problems, the coarsening of the grid in the radiator and bypass areas was done using the same grid topology and with small gradual increments in cell size.

The simplest of the complete turbulence models are two-equation models in which the solution of two separate transport equations allows the turbulent velocity and length scales to be independently determined. The standard k-ε model in FLUENT falls within this class of turbulence models and has become the workhorse of practical engineering flow calculations in the time since it was proposed by Launder and Spalding[22]. Robustness, economy, and reasonable accuracy for a wide range of turbulent flows explain its popularity in industrial flow and heat transfer simulations. It is a semi-empirical model, and the derivation of the model equations relies on phenomenological considerations and empiricism.

Table 1
Cartesian location of pressure tappings (in mm)

| Tap	x-co-ord	y-co-ord	Tap	x-co-ord	y-co-ord	Tap	x-co-ord	y-co-ord
1	−10	0	18	15	25·9	35	70	0
2	5	8·7	19	30	0	36	60·6	−35
3	10	0	20	25·9	−15	37	0	−70
4	8·7	−5	21	0	−30	38	−35	−60·6
5	0	−10	22	−15	−25·9	39	−60·6	−35
6	−5	−8·7	23	−25·9	−15	40	−50	86·6
7	−8·7	−5	24	−45	0	41	50	86·6
8	−20	0	25	22·5	38·9	42	100	0
9	10	17·3	26	45	0	43	86·6	−50
10	20	0	27	38·9	−22·5	44	0	−100
11	17·3	−10	28	0	−45	45	−50	−86·6
12	0	−20	29	−22·5	−38·9	46	90	155·9
13	−10	−17·3	30	−38·9	−22·5	47	180	0
14	−17·3	−10	31	−70	0	48	155·9	−90
15	−30	0	32	−60·6	35	49	90	155·9
16	−25·9	15	33	0	70			
17	0	30	34	35	60·6			
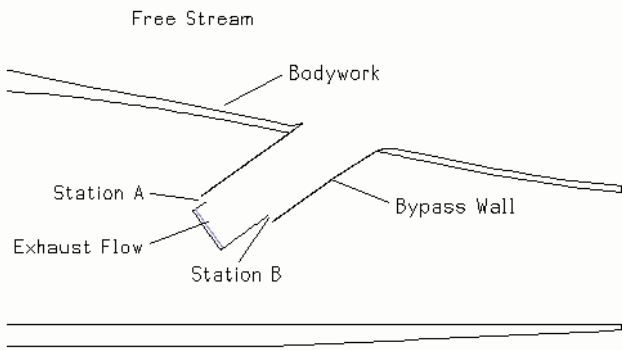
Figure 3. Cross-sectional view of exhaust and bodywork configuration.

An extensive recent review on the strengths and weaknesses of turbulence models as well as their practical applicability can be found in the article by Leschziner and Drikakis[23]. From their investigations, it can be concluded that linear eddy-viscosity models are fundamentally flawed and often perform poorly in flows featuring separation, strong shock/boundary-layer interaction and 3D vertical structures. In general, 2-equation turbulence models, such as the k-ε or k-ω, return disappointing results in the simulation of curved flows. On the other hand, more computationally expensive models, like the Reynolds Stress Transport Models, have proven to be excessively complex for most practical cases, and similar results can be obtained with a conveniently modified 2-equation model. Further assessments of design properties of different turbulence models can be also found in Refs 24 and 25.

Grid and model sensitivity analysis is performed in order to find a good compromise between numerical accuracy and computational cost of the simulations. The predictions from three different turbulence models, i.e. Standard k-ε, RNG k-ε and Reynolds Stress Transport were compared and at the same time a grid sensitivity analysis was performed for each of them. The comparatively large scale of the flow domain with respect to the size of the aspiration duct of the exhaust pipe suggested that a double precision solver should be employed over a single precision one.

The strengths and limitations of the standard k-ε model are well known nowadays; therefore variants to improve its performance have been made, such as the Renormalisation Group (RNG)[26] or the Realisable k-ε[27]. Whereas the latter presents major strengths in solving the spread rate of a jet, the RNG k-ε is mainly employed for rapidly strained flows. In the present case study, the area of interest is formed by a relatively small and short passage, where a high velocity gradient exists, thus suggesting high strain levels in the flow.
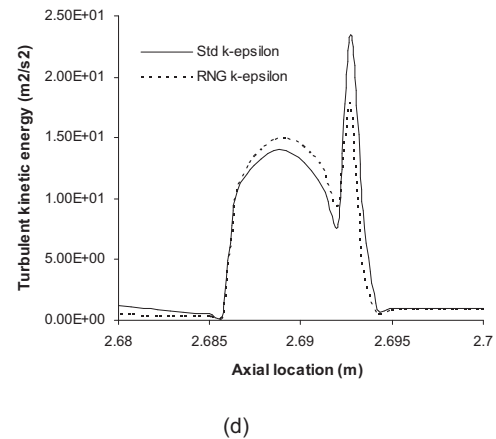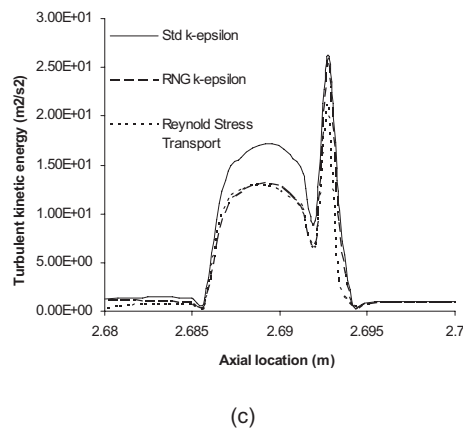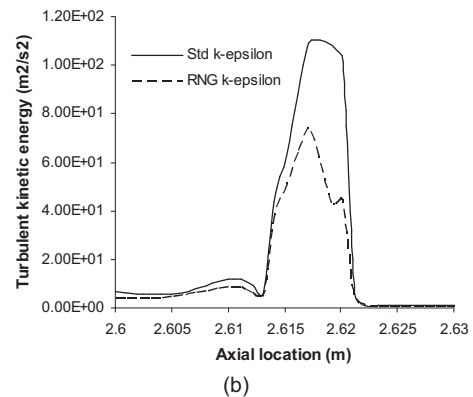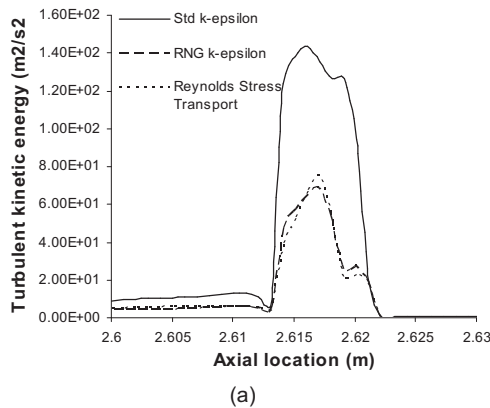

(a)

(b)

(c)

(d)

Figure 4. (a) Effect of turbulence model on the prediction of turbulence kinetic energy through the upper bypass with a 16-node grid. (b) Effect of turbulence model on the prediction of turbulence kinetic energy through the upper bypass with a 32-node grid. (c) Effect of turbulence model on the prediction of turbulence kinetic energy through the lower bypass with a 16-node grid. (d) Effect of turbulence model on the prediction of turbulence kinetic energy through the lower bypass with a 32-node grid.

Based on the results obtained from the grid and model sensitivity analysis, RNG k-ε was employed to model turbulence. A grid was designed such that it would contain 16 nodes between the walls of the bypass, as it was found to produce reasonable accurate results without having to resolve detailed physics of the near wall region, which, on the other hand, is not the objective of the present work. From a mathematical point of view, the difference between the standard k-ε and the RNG resides in a modified expression for the turbulence viscosity.

$$\mu_t = \mu_{to} f\left(\alpha_s, \Omega, \frac{k}{\varepsilon}\right) \qquad \ldots (4)$$

This is reflected with the addition of an extra term in the diffusion equation and is given by

$$R = \frac{c_\mu \eta^3 \rho \left(1 - \eta/\eta_0\right)\varepsilon^2}{1 + \beta\eta^3} \qquad \ldots (5)$$

where $\eta_o = 4\cdot38$, $C\mu = 0\cdot0845$, $\beta = 0\cdot012$ are the model constants.
Therefore, the transport equations can be rearranged to give

$$\rho\frac{Dk}{Dt} = \frac{\partial}{\partial x_i}\left(\alpha_k \mu_{eff} \frac{\partial k}{\partial x_i}\right) + G_k - \rho\varepsilon \qquad \ldots (6)$$

$$\rho\frac{D\varepsilon}{Dt} = \frac{\partial}{\partial x_i}\left(\alpha_\varepsilon \mu_{eff} \frac{\partial\varepsilon}{\partial x_i}\right) + C_{1\varepsilon}\frac{\varepsilon}{k}G_k - C_{2\varepsilon}\rho\frac{\varepsilon^2}{k} - R \qquad \ldots (7)$$

where x_i represents the tensor notation for spatial direction and $C_{1e} = 1\cdot42$ and $C_{2e} = 1\cdot68$ are the model constants.
The term for the production of turbulence kinetic energy, TKE, is represented by G_k and is computed in the same manner in all of the variants of the k-ε model;

$$G_k = -\rho\overline{u_i \cdot u_j}\frac{\partial u_j}{\partial x_i}$$

These transport equations were numerically approximated by application of a Second Order Upwind discretisation method. FLUENT employs a control volume method to convert the partial differential equations into algebraic equations in order to obtain numerical results. The governing equations are integrated over the control volume to yield discrete equations that conserve each quantity on a control volume basis. Equation (8) represents the steady state transport equation for a generic scalar quantity ϕ over a control volume V.

$$\oint \rho\phi\vec{v}\cdot d\vec{A} = \oint \Gamma_\phi \nabla\phi\cdot d\vec{A} + \int_V S_\phi \, dV \qquad \ldots (8)$$

where ρ is the density, $\vec{v}$ is the velocity vector, $\vec{A}$ is the surface area vector, Γ_ϕ is the diffusion coefficient of scalar Φ, $\nabla\phi$ is the gradient of Φ and S_Φ is the source of Φ per unit volume.
This transport equation is applied to each control volume, or cell, in the computational domain, and its discretisation on a given cell can be expressed as

$$\sum_f^{N_{faces}} \rho_f \vec{v}_f \phi_f \cdot \vec{A}_f = \sum_f^{N_{faces}} \Gamma_\phi \left(\nabla\phi\right)_n \cdot \vec{A}_f + S_\phi V \qquad \ldots (9)$$

where N_{faces} is the number of faces enclosing a cell, ϕ_f is the value of Φ convected through face f, $\rho_f \vec{v}_f \cdot \vec{A}_f$ is the mass flux through the face; $\vec{A}_f$ is the area of the face, $(\nabla\phi)_n$ is the value $\nabla\phi$ of normal to face f and V is the cell volume.
The upwind method employed to discretise the transport equations means that the face value of a scalar is computed from quantities in the cell upstream the face considered. In the case of Second Order Upwind, as used in the present work, quantities at cell faces are computed using a multidimensional linear reconstruction approach. Higher order accuracy than First Order Upwind is achieved through a Taylor series expansion of the cell-centered solution about the cell centroid. When second-order upwinding is employed, the face value of the scalar is computed as shown in Equation (10), where Φ and $\nabla\phi$ are the cell-centered value and its gradient in the upstream cell, and $\Delta\vec{s}$ is the displacement vector from the upstream cell centroid to the face centroid.

$$\phi_f = \phi + \nabla\phi\cdot\Delta\vec{s} \qquad \ldots (10)$$

As a result, the cell gradients must be computed in each cell. In the current solver this is computed using the divergence theorem, which in discrete form can be written as

$$\nabla\phi = \frac{1}{V}\sum_f^{N_{faces}} \tilde{\phi}_f \vec{A} \qquad \ldots (11)$$

In this expression, the face values have been computed by averaging from the two cells adjacent to the face.
The boundary conditions were defined as follows: free stream velocity $67\cdot1\text{ms}^{-1}$, exhaust gas velocity $59\cdot73\text{ms}^{-1}$ and a porous jump boundary was used to simulate the radiator, for which a face permeability of $1\cdot95\text{e}^{-05}\text{m}^2$, a porous medium thickness of $0\cdot055\text{m}$ and pressure jump coefficient of 185l/m were employed. The convergence criterion employed in the scalar transport equations solved in both the 2 and 3-dimensional studies was based on residual values of 10^{-3} for each transport equation, in all cases.

4.0 RESULTS

4.1 Turbulence model and grid sensitivity analysis

The grid refinements were concentrated around the exhaust and bypass area, increasing the number of nodes between the exhaust pipe and the bypass duct. The most significant results were obtained with 16 and 32-node grids. Figure 3 depicts a cross sectional view of the rear part of the generic formula one car assembly as it was simulated in the solver. In the present case, we have investigated the sensitivity to three different turbulence models: standard k-ε, RNG k-ε and Reynolds Stress Transport, Fig. 4. In general, the latter is a more accurate model but is more computationally expensive than any of the k-ε. For this reason, the Reynolds Stress Transport model (RST) will be taken as a reference for accuracy of the simulation. In Figs 4(a) and 4(b), the turbulence kinetic energy along the width of the upper bypass duct, station A, is plotted for 16-node and 32-node grids respectively. The graphs show a close similarity between the RNG k-ε and the RST, whilst the standard k-ε seems to overpredict the turbulence kinetic energy with respect to the other two models. A similar pattern of behaviour is observed on station B (lower bypass) in Figs 4(c) and 4(d), although differences are not as acute. By comparison of the graphs from the 16-node and the 32-node grids, it was also seen that the gain in accuracy of the results achieved through the refinement of the mesh was very small. This model and grid sensitivity analysis suggested that the best compromise between accuracy and computational cost would be achieved with a 16-node grid and the RNG k-ε model.

4.2 Exhaust-aerofoil interference

Figures 5 to 8 depict the lift coefficient acting on the aerofoil at 32, 45, 60 and 90mm above the ground respectively. Although only the 45mm configuration represents a parametric copy of the real F1 car configuration, the other aerofoil heights are tested in order to monitor the effect of the dissipation of the jet in the free stream on the lift coefficient acting on the wing element. Although positive and
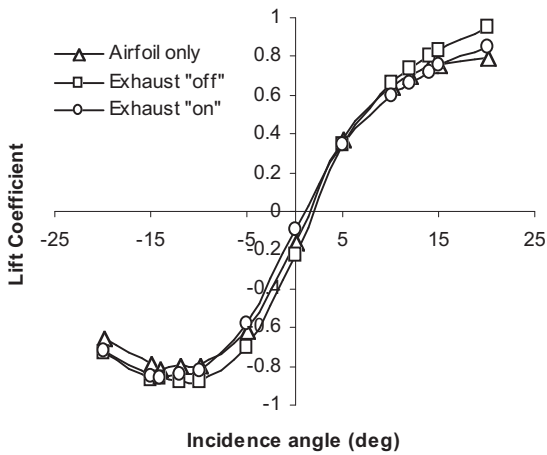
Figure 5. Lift coefficient with aerofoil placed 32mm above the floor of the wind tunnel.
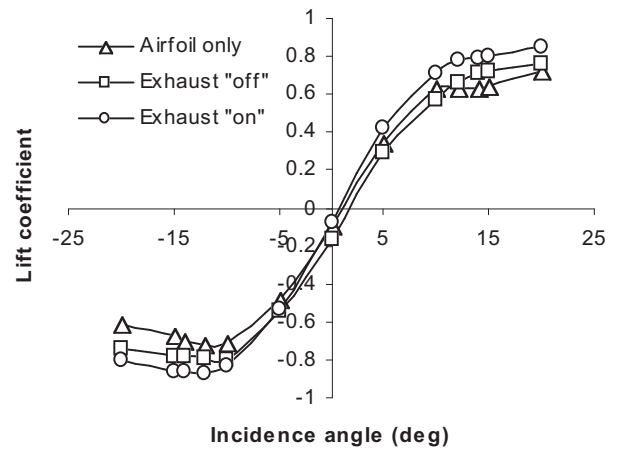

Figure 6. Lift coefficient with aerofoil placed 45mm above the floor of the wind tunnel.
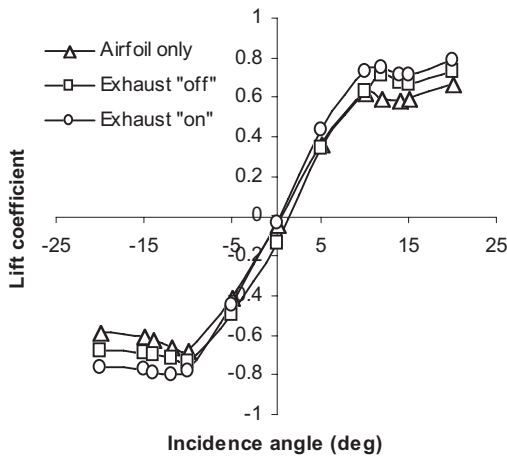

Figure 7. Lift coefficient with aerofoil placed 60mm above the floor of the wind tunnel.
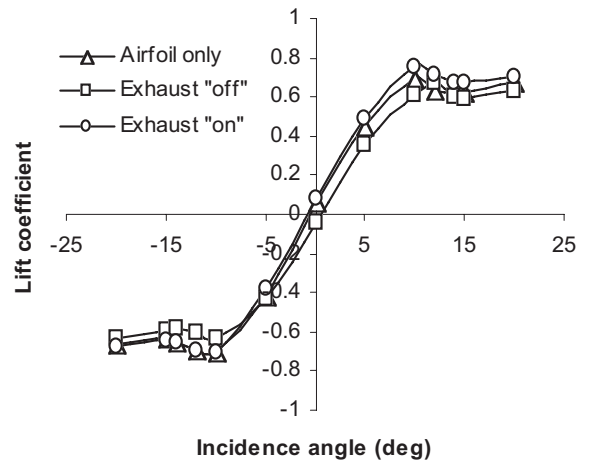

Figure 8. Lift coefficient with the aerofoil placed 90mm above the floor of the wind tunnel.
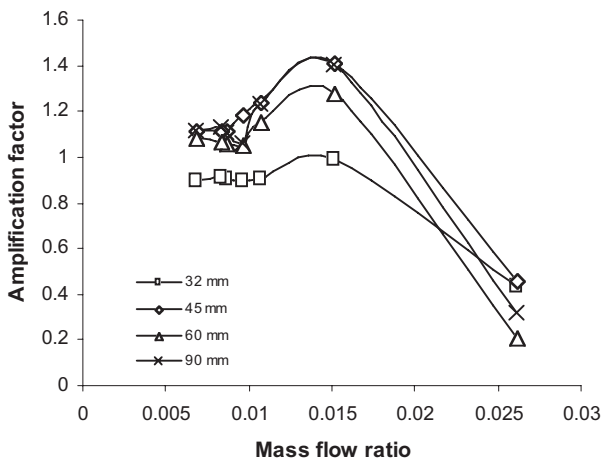

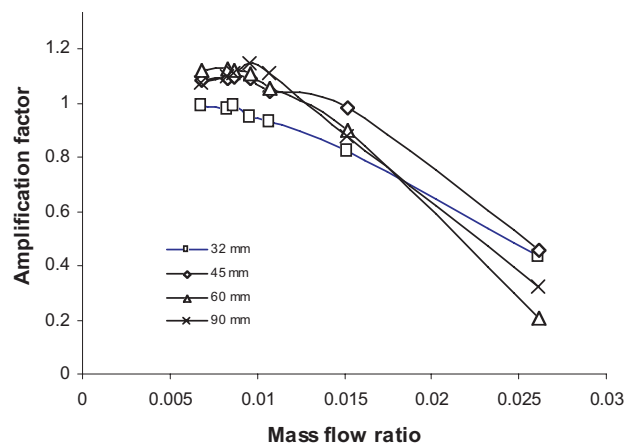Figure 9. Amplification factor vs. mass flow ratio for various aerofoil heights (incidence range 0° to –20° degrees).

Figure 10. Amplification factor vs. mass flow ratio for various aerofoil heights (incidence range 0° to +20° degrees).

negative incidences have been studied, it is important to note that in Formula One, positive incidence angle are never used on the wing elements. Therefore, the discussion will focus mainly in the area of the graph referring to the negative incidence angle.

Figure 5 shows that the presence of the car body causes a slight negative lift on the aerofoil at zero degrees incidence. This could be due to the generation of a low pressure area downstream the car body, see Figs 11 and 12, therefore leading to a slight increment in the flow velocity in that area. Consequently, the pressure coefficient on the lower surface of the aerofoil will be smaller in value than that on the upper surface, which leads to the generation of a negative lift on the aerofoil.

Another feature of this graph is the fact that the absolute value of the lift coefficient acting on the aerofoil was increased by the presence of the car body for the entire range of incidence angles. The improvement in the aerodynamic lift on the aerofoil when the car body is introduced resides in the increment of the ground surface over which the fluid has to travel. The attachment of the bodywork model, as described above, implies that the total contour of the floor of the wind tunnel is longer than the top surface. This effect is reinforced by the fact that the car body behaves as a perfect streamlined body at the flow speeds considered during the experiment, as observed in the oil flow experiments, Fig. 14. As a result of this velocity distribution, the air flowing beneath the aerofoil travels faster than the flow on the top surface, hence generating a negative lift, or downforce. This effect is reinforced as the incidence is modified in both positive and negative directions. This can be explained by looking at the attachment of the aerofoil by the ¼ chord, meaning that the distance from the trailing edge of the aerofoil to the connecting rod is three times longer than the distance to the same point from the leading edge. The implication of this feature is based on the different cross sectional areas left underneath the aerofoil when the aerofoil rotates the same amount of degrees on the positive or negative side. Positive angle rotation will 'squeeze' the flow between the trailing edge and the lower surface of the wind tunnel, eventually 'choking' (not in its true aerodynamic sense) the flow below the wing, resulting in an increment of the positive lift. On the other hand, when the aerofoil is rotated to a negative angle of incidence, the leading edge is not long enough to choke the flow, although it generates a throttling effect between this edge and the floor of the wind tunnel, i.e. a flow acceleration in the contraction area, which tends to increase the downforce recorded due to the proximity of the attachment point of the aerofoil. Such throttling will be followed by a flow deceleration, as the trailing edge of the wing acts as a diffuser.

Although the exhaust flow also increases the lift relative to the aerofoil only configuration, it reduces the aerofoil performance with respect to the 'exhaust-off' configuration. This effect, only observed in this particular configuration, is due to the fact that the aerofoil lies below the main stream of the exhaust jet. As a result, the exhaust flow tends to travel along the upper surface of the aerofoil for negative incidence angles and below the aerofoil for positive incidence angles. In both cases, the ultimate outcome is a decrease in the absolute value of the lift coefficient acting on the wing with respect to that of exhaust-off configuration. In the case of zero degrees incidence, the lift values recorded in all three configurations are very similar. Thence it can be deduced that at this incidence position the exhaust stream is impinging somewhere near the leading edge of the aerofoil and that approximately the same amount of exhaust gas flows over the upper and the lower surfaces of the aerofoil.

Figure 6 depicts the lift coefficient recorded when the aerofoil is placed 45mm above the floor of the wind tunnel. In this case the benefits of the extra flow, coming from the exhaust, on the lift coefficient acting on the aerofoil are clearly visible. The exhaust jet increases the downforce on the wing by approximately 10% for incidence angles between −10° and −20°. This result would be considerably beneficial if applied to a Formula One car, as the

apparent weight of the vehicle could be increased and, as a result, the grip on the tyres will be enhanced. The remaining aerofoil positions tested reveal a decreasing effect of the exhaust jet on the lift force on the aerofoil. Nevertheless, this effect was still clearly observed when the aerofoil was placed 60mm above the floor of the wind tunnel, as shown in Fig. 7.

Besides the increment in downforce, another important effect of the exhaust flow on the aerofoil aerodynamic behaviour is clearly observed at 45 and 60mm above the ground. The extra flow delays and smoothes the appearance of aerodynamic stall, whereas in most cases avoiding aerodynamic stall is one of the main objectives of aerofoil design; mainly because this effect causes a drop in the aerodynamic lift of an aerofoil. Therefore, this can be considered as a second advantage of orientating the exhaust gases toward the rear wing.

Aerodynamic stall can still be observed in the first case, 32mm above the ground, Fig. 5 and the final case, 90mm above the ground, Fig. 8. However, in the first case it is only visible within the negative incidence zone, due to 'choked' flow in the positive incidence range.

Figure 8 also shows small exhaust-wing interference, mainly due to the dissipation of the momentum of the jet. In order to have a better idea on how the exhaust flow interferes with the aerofoil and affects its performance, the mass flow rate ratio between the free stream and the exhaust has been plotted against the amplification factor, Figs 9 and 10.

$$Mass\_flow\_ratio = \frac{U_{jet}}{U_{free-stream}} \cdot \frac{d_{jet}^2}{A} \qquad \ldots (12)$$

where A is the wetted area of the aerofoil, which can be given as a function of the incidence angle by

$$A = s \cdot (t_a + c \cdot \sin \alpha) \qquad \ldots (13)$$

The amplification factor is given by the ratio between the forces acting on the aerofoil when the exhaust is activated and the forces with no exhaust flow:

$$K = \frac{L_{(exhaust-on)}}{L_{(exhaust-off)}} \qquad \ldots (14)$$

Figure 9 depicts the amplification ratio for the four aerofoil heights tested and the negative range of incidences, i.e. 0 to -20 degrees. From these curves it can be deduced that the performance of the aerofoil at the lowest position does not benefit at any time from the presence of the exhaust jet, with amplification factors always below unity. In contrast, the amplification factor for the remaining aerofoil positions was above unity at all incidences before aerodynamic stall appeared. When the negative incidence is increased, in absolute value, the flow underneath the aerofoil tends to separate earlier, disrupting the velocity difference between the two sides of the aerofoil, which ultimately causes the negative lift coefficient. Nevertheless, the exhaust jet provides a small stream underneath the aerofoil, increasing the local velocity and, hence the downforce. This could explain the increasing effect of the jet in the amplification factor until stall point is reached.

In the case of positive incidence variations, Fig. 10, the behaviour of the amplification factor is very similar for all cases. For small incidences, the amplification factor remains close to unity, and, as the incidence is increased, the aerodynamic lift decays. The exhaust jet tends to form a stream near the lower surface of the aerofoil. At positive incidence this reduces the aerodynamic lift of the wing, because the lower surface of the wing section is now in the wind side, which needs to keep flow velocities as low as possible in order to increase the lift.

The effect of the exhaust jet on the pressure ratio (P/P_∞) distribution on the car body was also studied. The pressure registered by the pressure transducers was recorded for both exhaust-on and exhaust-off

configurations. Figure 11 depicts a comparison of the pressure ratios on the car body along the centreline, which passes through the exhaust pipe, hence the discontinuity of the curve. The results show an area of higher pressure ratio in the leeward side of the exhaust jet. In JICF, this is an area of high vorticity, with relatively low flow velocities, that leads to higher static pressure values.

Figures 12(a) and 12(b) depict the pressure maps on the car body with and without the influence of the jet. The centre of the exhaust pipe is located at $(x,y) = (0,0)$ and negative values have been assigned to the zone of the car body upstream the exhaust exit. The drop in pressure ratio near the exit of the exhaust is due to the accelerating free stream flow, which needs to surround the exhaust jet.

Figure 12(a) shows that the presence of the jet exhaust jet orifice exerts a slight influence in the pressure levels recorded. Figure 12(b), reveals the presence of two high pressure ratio zones, one in the leeward side of the jet and one in the windward side. The one in the windward side of the jet is due to the presence of a free stagnation point formed as a result of the blockage generated by the issuing jet. The high pressure zone in the leeward side of the jet is due to the high mixing, where recirculating flow occurs on the surface of the body, see Fig. 15. It can also be identified in Fig. 12(b), the formation of a horseshoe vortex. The experimental uncertainty in the pressure and lift results discussed in Section '2 Experimental equipment and procedure' justify the conclusions drawn from the experimental measurements.

4.3 Oil flow study

The oil flow technique was employed in order to visualise the mixing and separated areas of the flow. Given the difficulty of applying oil flow to the lower surface of the aerofoil, this technique was applied to the car body and the upper surface of the wing only.

Figure 13 shows the oil flow on the aerofoil at zero degree incidence, placed 45mm above the floor and in exhaust-off configuration. The main features of this picture are the separation line found about 2/3 of the chord downstream the leading edge and the 'mushroom-shaped' flow field near the trailing edge. Also visible in Fig. 13 is a recirculation area around the left hand side end of the aerofoil. This is caused by the opening made in the side wall of the wind tunnel to allow the vertical motion of the aerofoil.

Figure 14 depicts the behaviour of the free stream flow along the model car body when the exhaust is off. It is interesting to notice the highly streamlined design of the body, which shows no signs of flow separation. This result would be in accordance with the discussion in the previous section, in which it was mentioned that the car body does not exert a blockage on the free stream flow. The small white dots visible are caused by the accumulation of oil and TiO_2 around the pressure tappings.

The effects of the exhaust flow are visible in the close-up image depicted in Fig. 15. The stream lines surround the exhaust jet and convect immediately downstream the exhaust exit. This causes two mixing wakes that run along parallel to the free stream flow.

The free stream flow does not mix instantaneously with the exhaust flow, which behaves as a deformable solid in the near region. As a result, the free stream must surround the exhaust jet, thence the semicircular path-lines. The stagnation region seen in the windward side of the jet in Fig. 15 has been referred to as free stagnation point. A visual comparison between the oil flow results shown in Figs 14 and 15 indicates clearly that the distance that the free stream flow must travel with the exhaust flow operative is longer than that in the exhaust-off configuration, causing as a result flow acceleration upstream the exhaust exit. A close analysis of Fig. 15 reveals small vortices occurring along the sides of the core of the exhaust jet. This feature is characteristic of the flow downstream of a solid object, where re-circulating flow and low velocities are recorded, and therefore the higher pressure ratio depicted in Fig. 12.
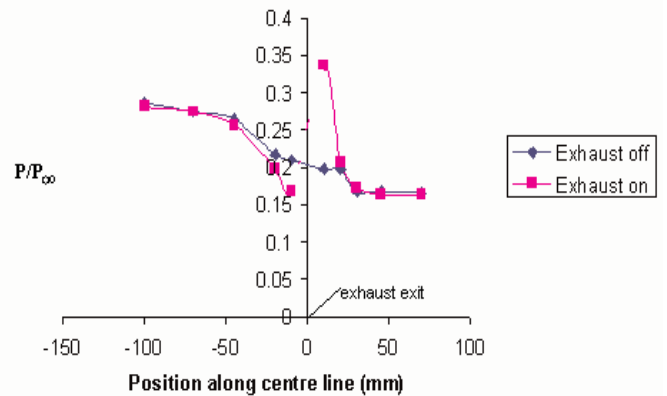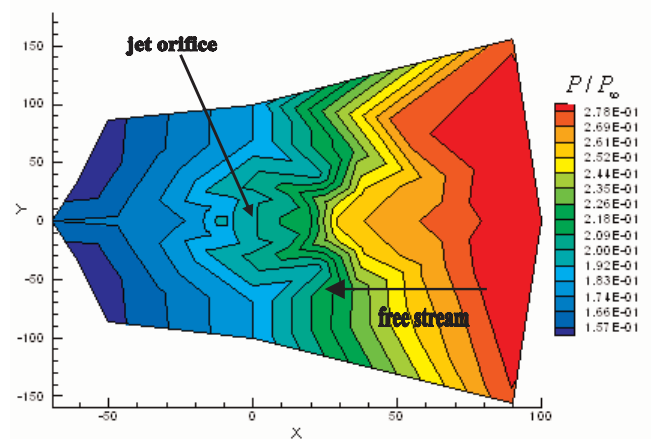

Figure 11. Exhaust-bodywork interference.

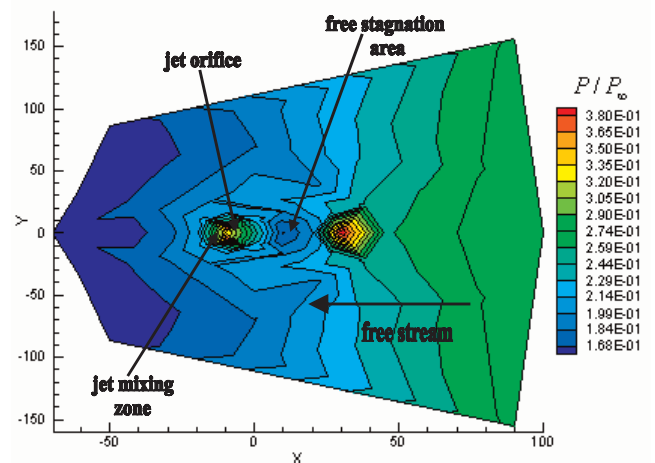Figure 12(a). Pressure contours on car body with exhaust off.

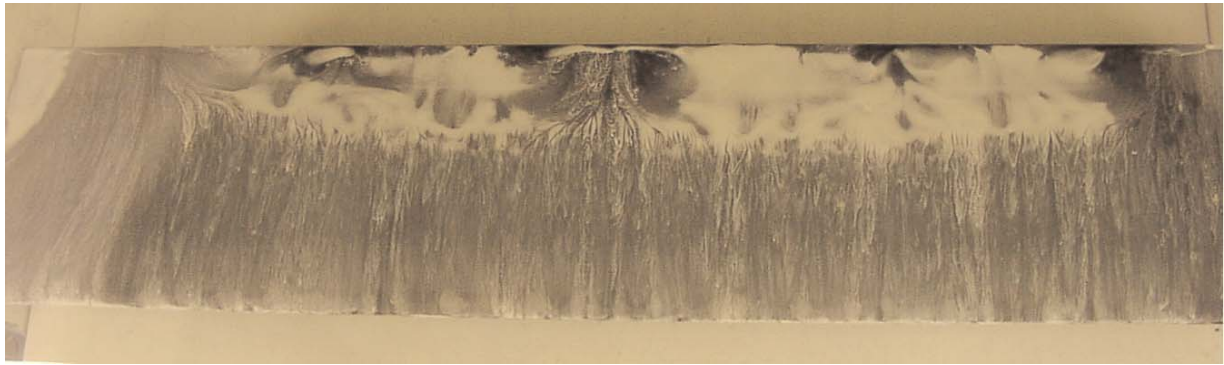Figure 12(b).Pressure contours on car body with exhaust on.

Figure 13. Oil flow on aerofoil, exhaust off.
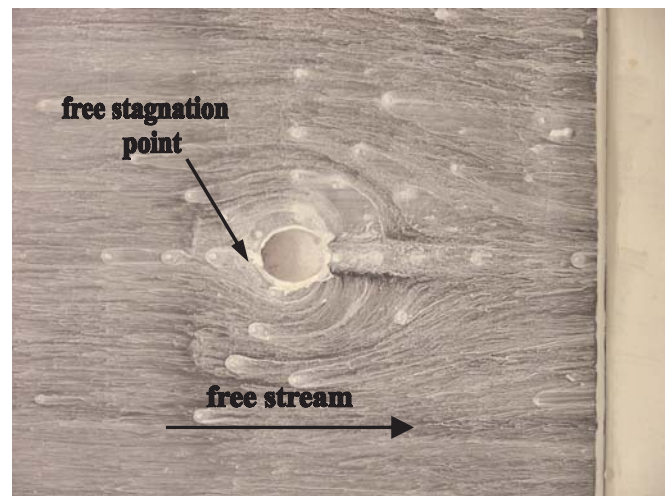

Figure 14. Oil flow on car body, exhaust-off.

Figure 15. Detail of exhaust exit area.

4.4 Computational results

4.4.1 2-dimensional study

The 2-dimensional simulation comprised the analysis of the influence of relative overlap variations between the exhaust pipe and the bypass duct and, thereafter, the influence of the exhaust pipe/bypass diameter
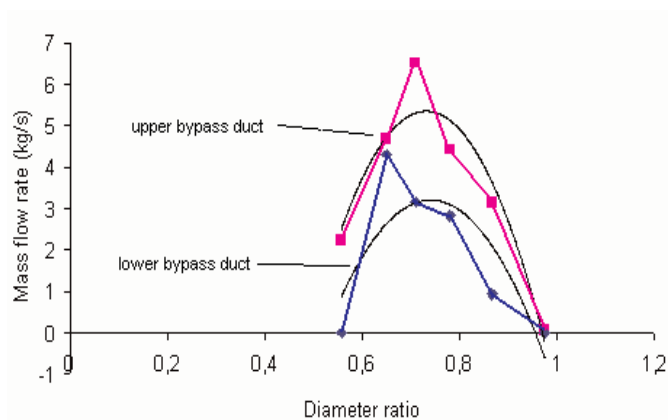

Figure 16. Effect of the diameter of the bypass on the mass flow rate of aspirated gases through the bypass.

ratio on the aspiration generated by exhaust gases. Because this study has clear 3-dimensional connotations, the 2-dimensional results are primarily aimed to the identification of significant trends in the physical behaviour of the flow. This approach reduced the number of 3-dimensional simulations, which required significantly higher computational effort than the 2-dimensional simulations.

In this part of the study, there are two factors to account for separately: the diameter ratio of the exhaust pipe and the duct inside which exhaust gases are expelled (referred to as bypass) and the relative overlap between the exhaust pipe and the bypass.

Figure 16 depicts the effect of the diameter ratio (d_{jet}/d_{bypass}) on the aspiration of air through the bypass. The solid curves represent a polynomial approximation of the results obtained from the simulation. Because the diameter of the exhaust cannot be modified (due to the rules imposed by the motor sport governing body, FIA[19], the diameter ratio was modified by increasing or decreasing the diameter of the bypass. The mass flow rate was computed on control lines defined at the upper and lower entries of the bypass duct. According to the simulations, a diameter ratio of about 0·75 yields a maximum aspiration through the bypass. Smaller bypass diameter means that the flow starts to choke inside the bypass, with the consequent drop in mass flow rate. On the other hand, greater diameter ratios can cause flow recirculation inside the bypass, adversely affecting the level of negative pressure gradient that would cause the aspiration of air through the passage. Figures 17(a) to 17(d) depict the effect of gradual increments to the diameter of the bypass duct. Due to the geometric characteristics of the design and the 2-dimensional nature of these simulations, the upper and lower bypass ducts reveal a different behaviour. The upper duct benefits from an increment in outer duct diameter (up to the point of doubling the original bypass diameter, Fig. 17(c) and its positioning favours the aspiration of
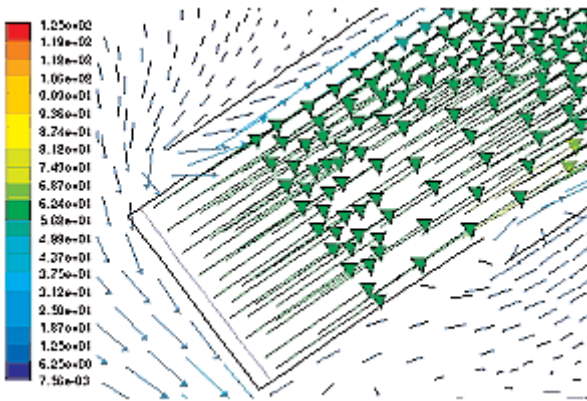
Figure 17(a) Direction velocity vectors at entry of
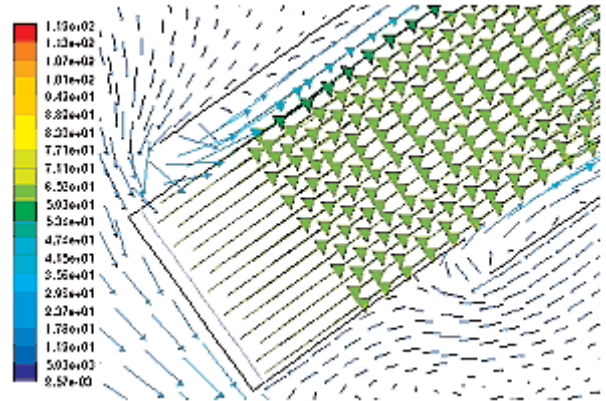bypass duct for original diameter ratio; $d_{bypass} - d_{exhaust} = d$.

Figure 17(b).Direction velocity vectors for 50%
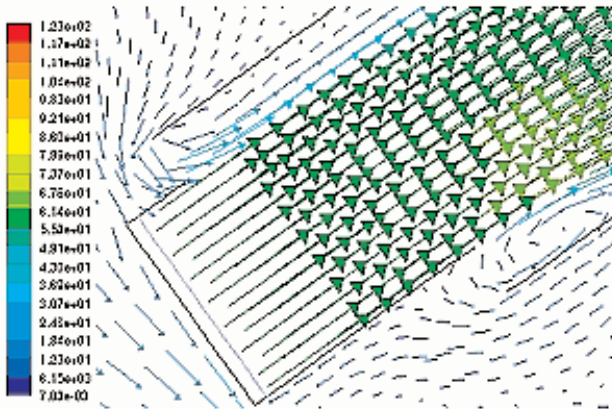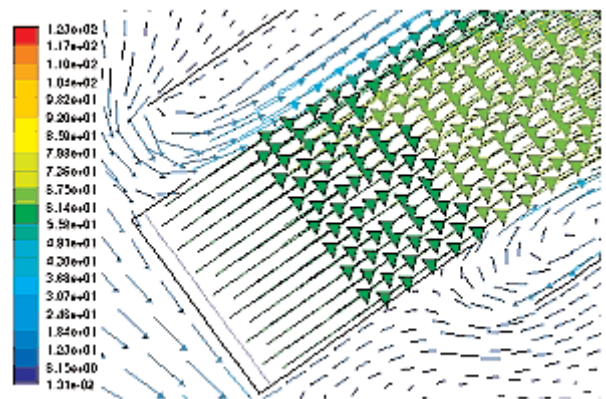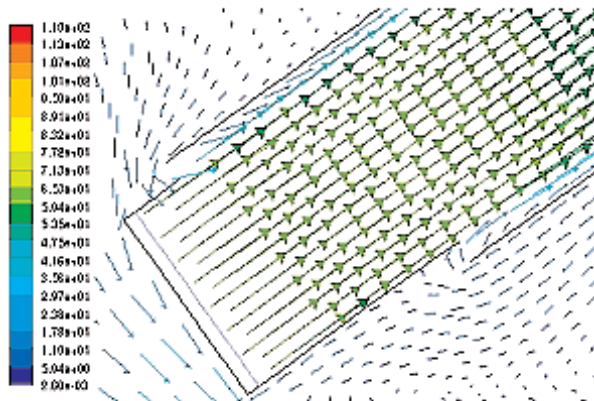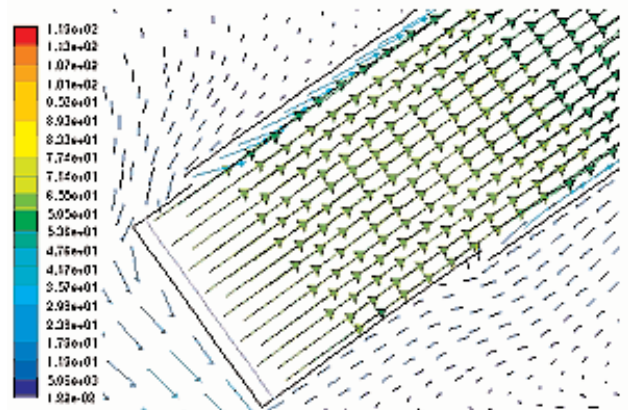increase aspiration duct width; $d_{bypass} - d_{exhaust} = 1{\cdot}5d$.

Figure 17(c).Direction velocity vectors for 100%
increase aspiration duct width; $d_{bypass} - d_{exhaust} = 2d$.

Figure 17(d). Direction velocity vectors for 200%
increase aspiration duct width; $d_{bypass} - d_{exhaust} = 3d$.

Figure 17(e). Direction velocity vectors for 50%
decrease aspiration duct width; $d_{bypass} - d_{exhaust} = 0{\cdot}5d$.

Figure 17(f).Direction velocity vectors for 75%
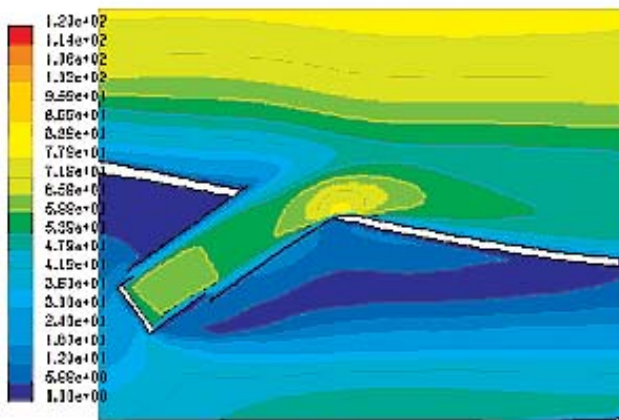decrease aspiration duct width; $d_{bypass} - d_{exhaust} = 0{\cdot}25d$.

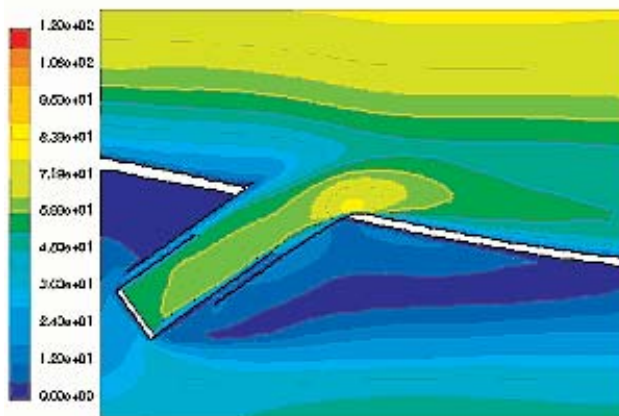Figure 18(a).Velocity contours around
the exhaust area at 0% overlap.

Figure 18(b).Velocity contours around
the exhaust area at 50% overlap.

Figure 18(c). Velocity contours around
the exhaust area at 100% overlap.

gases. On the contrary, the positioning of the lower bypass tends to create a vortex at the entry of the duct (primarily caused by the presence of the exhaust pipe), which ultimately reduces significantly the aspiration through this side, relative to the upper bypass. Recirculating flow is observed in the lower bypass, Figs 17(b) to 17(d). Nevertheless, an excessive opening between the exhaust pipe and the bypass yields recirculating flow at the entry of both the upper and the lower aspiration duct, as seen in Fig. 17(d)

The last two figures, Figs 17(e) and 17(f), depict the flow behaviour when the diameter of the bypass is reduced, firstly halved and then by 75%. In these cases, recirculation does not occur, but a gradual decrease of the aspiration momentum inflicted by the exhaust gases on the radiator chamber gases is observed.

Both upper and lower ducts produced maximum aspiration at diameter ratios between 0·62 and 0·7. It is reasonable to believe that the maximum aspiration is generated when the gap between the exhaust pipe and the outer duct is close to the thickness of the shear layer generated between the exhaust jet and the stagnant air in the bypass ducts. As a result, decreasing the space available for the development of the shear layer implies a reduction in the mixing of the exhaust gases with the surrounding fluid, see Fig. 15.

The velocity contours around the exhaust area are depicted for three different exhaust-bypass overlap configurations: 0% overlap (Fig. 18(a), 50% overlap (Fig. 18(b)) and 100% overlap (Fig. 18(c)). Although these are valid for qualitative analysis purposes only, some differences in the physical behaviour of the exhaust jet can be observed. Figures 18(a) and 18(b) show shear layers along the sides of the core of the exhaust jet, which indicate that entrainment by the surrounding fluid is taking place in those areas. Such mixing areas can also be observed in Fig. 18(c). However, in this case, the entrainment takes place between the exhaust jet and the free stream, hence not exerting a great effect on the aspiration of gases through the bypass. On the contrary, in the mixing layers depicted seen in Figs 18(a) and 18(b), the surrounding fluid constitutes part of the relatively stagnant air behind the radiator. As a result, aspiration of this air would enhance the performance of the radiator by increasing the air mass flow rate across the heat exchanger.

The amount of relative overlap can be altered by either shortening the bypass walls or shortening the exhaust pipe into the car. A superficial analysis of both situations outlines that when the exhaust remains at full length, the jet is being directly injected into the free stream. In order to clarify this point and to better understand the approach adopted let us consider the following notation:

Flow 1   →   Free Stream

Flow 2   →   Exhaust flow

Flow 3   →   Radiator chamber flow

In order to optimise the aspiration through the bypass, the mixing between flow 2 and flow 3 must be enhanced. In this situation, the flow 1 exerts a detrimental effect in the aspiration, because all the exhaust flow that mixes with it will not pull the air out from the radiator chamber. As a result, the closer the end of the exhaust pipe is to the free stream, the more difficult it will be to improve the aspiration, regardless of the amount of overlap. This happens simply because the mixing between flow 2 and flow 3 does not exist. The results obtained from FLUENT support this theory, and when the exhaust was at full-length, the aspiration did not vary much with the overlap ratio.

One other feature visible in Figs 18(a), 18(b) and 18(c) is the deformation experienced by the exhaust jet due to the interaction with the free stream. As a result of this interaction, the exhaust jet is pushed against the lower side of the bypass (Figs 18(a) and 18(b) or exhaust pipe (Fig. 18(c))). In the first two cases, the exit of the lower side of the bypass causes Coanda flow in the exhaust jet. In consequence, the jet flow remains attached to the upper surface of the bodywork. On the contrary, flow separation and recirculation (Fig 19) is observed when the exhaust gases are expelled directly into the free stream. A more concise visualisation of the behaviour of the flow around the shear layer generated by the exhaust jet is depicted in Figs 20(a) (0% overlap), 20(b) (50% overlap) and 20(c) (100% overlap).
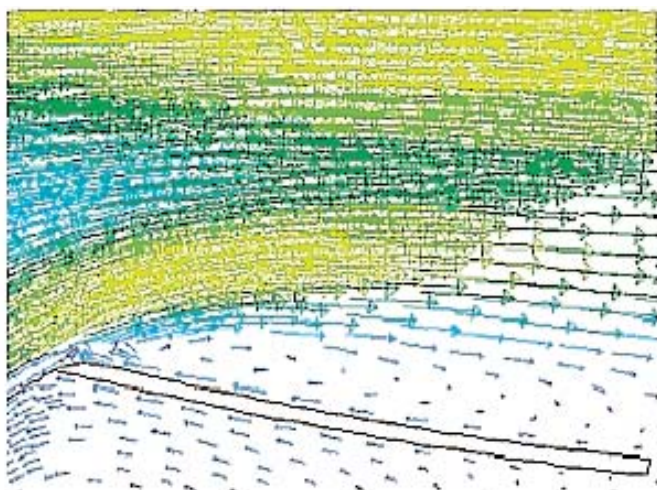
Figure 19. Direction vectors of velocity magnitude which show flow recirculation when the exhaust gases are expelled into the free stream.
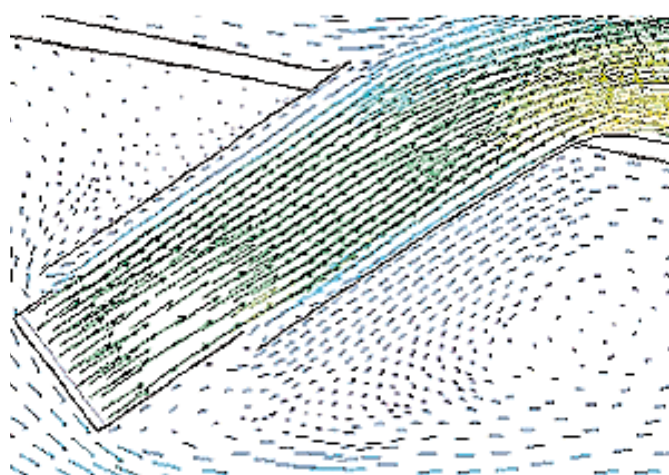

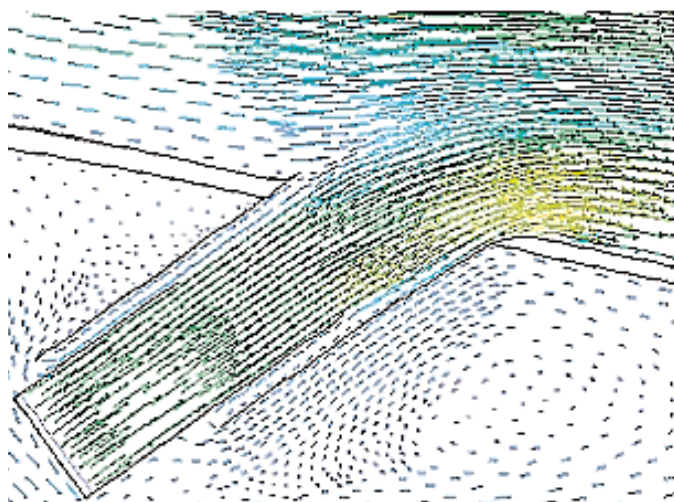Figure 20(a). Direction vectors of velocity magnitude, 0% overlap.

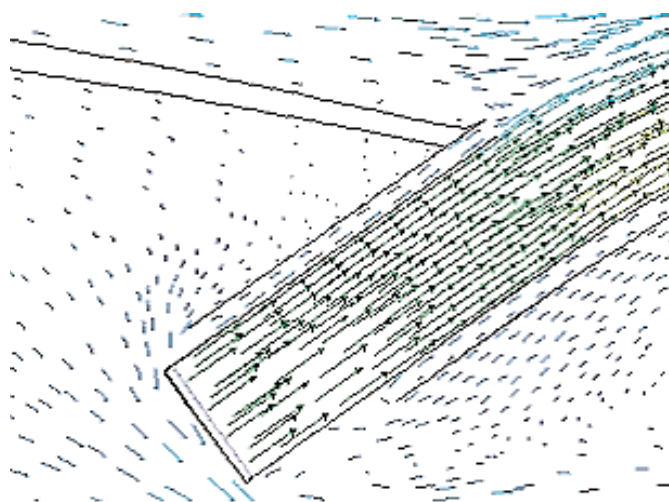Figure 20(b). Direction vectors of velocity magnitude, 50% overlap.

Figure 20(c). Direction vectors of velocity magnitude, 100% overlap.

Shortening the exhaust pipe implies an increment in the length allowed for the mixing between exhaust and radiator chamber to develop (mixing chamber). It is in this situation when the amount of overlap becomes an influencing factor for the aspiration. However, there is another issue to be considered, and this is the fact that making the exhaust shorter not only varies the distance allowed for mixing, but at the same time reduces the amount of overlap. In order to quantify the effects of each one of these parameters, a full case study with all the possible combinations of overlap and mixing chamber length should be performed. Such analysis was considered unfeasible due to the limited amount of time allocated to the 2-dimensional case study. Thus, the analysis was performed with constant bypass length and variable exhaust pipe. The results from these simulations are shown in Fig. 21. Note that in this case it does not make a difference to plot the velocity or the mass flow rate as the inlet area remains the same for all the cases. The explanation for this behaviour is based on the time, i.e. length, required to fully mix the exhaust flow with the flow coming from the radiator chamber. Once this point has been reached, further elongations of the chamber allowed for mixing does not exert any considerable effect. In other words, it could be said that both flows reach a 'mixing equilibrium'.

4.4.2 3-dimensional modelling

The final part of the CFD study consisted of the 3-dimensional simulation four of the cases previously examined in the 2-dimensional simulations. In this part, only the relative overlap ratio between exhaust pipe and bypass duct was investigated.

For the 3-dimensional modelling an unstructured mesh, made up of 623,000 tetrahedral cells, was employed. As in the 2-dimensional study, the main focus of the study resided in the aspiration generated by exhaust gases. Therefore, special care was taken in designing the mesh around the exhaust and bypass areas. The flow velocity was monitored on four horisontal planes, which intersected the exhaust and the bypass at four different heights, i.e. 300mm, 320mm, 350mm and 400mm above the ground. These control plane locations were defined taking into account the different exhaust pipe lengths simulated and the need to visualise the velocity magnitude at the entry of the bypass duct. Figures 22 and 23 depict the velocity vectors on the control plane located 300mm above the ground. In order to enhance the clarity of the vector plots, the velocity contours on this control plane are also shown, including the solid boundaries of the exhaust pipe (dark inner cylinder) and the bypass duct (lighter outer cylinder). These results suggest a greater aspiration generated in the leeward side of the exhaust jet in
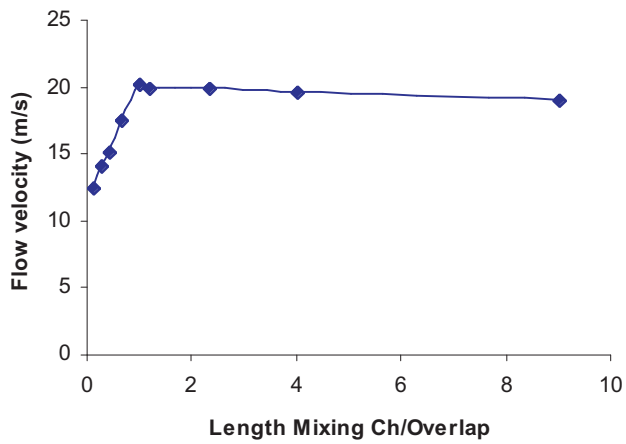
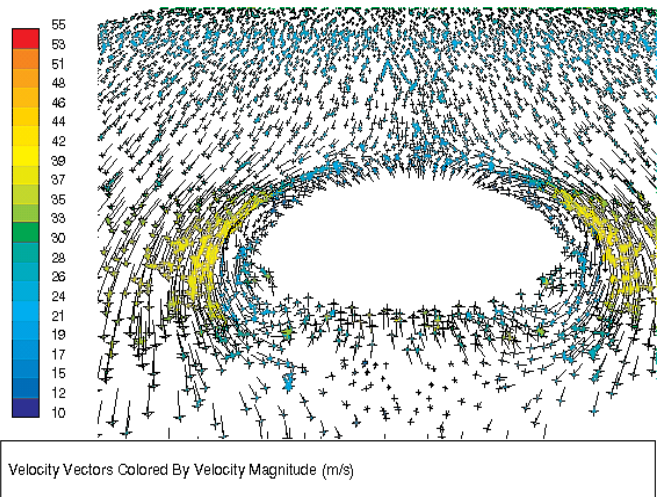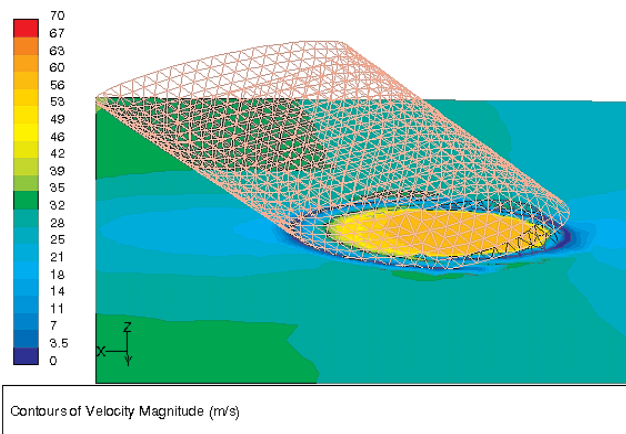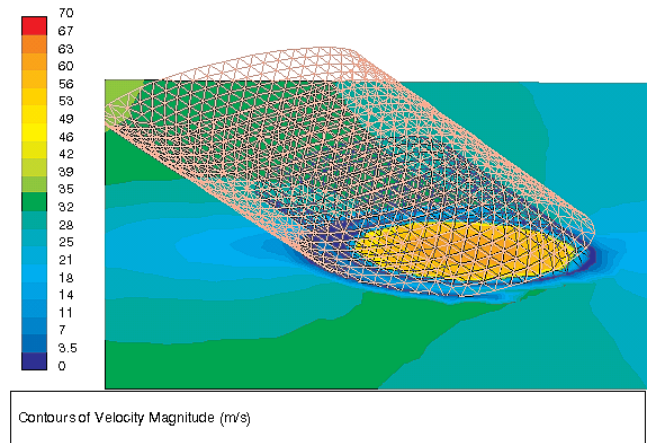Figure 21. Effect of length of exhaust pipe on aspiration.

Figure 23. Velocity magnitude contours and velocity
direction vectors on control plane 300mm (relative overlap 50%).
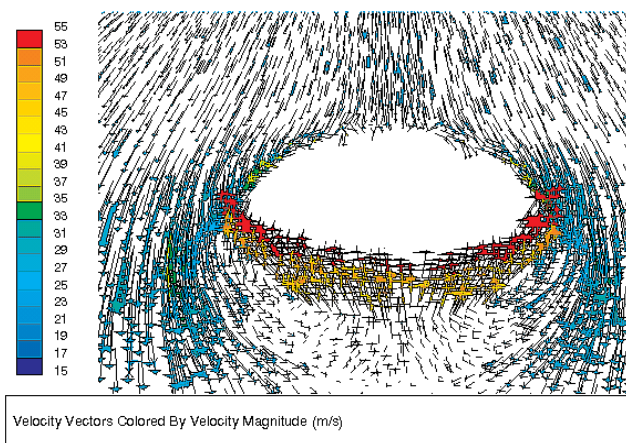

Figure 22. Velocity magnitude contours and velocity
direction vectors on control plane 300mm (relative overlap 0%).
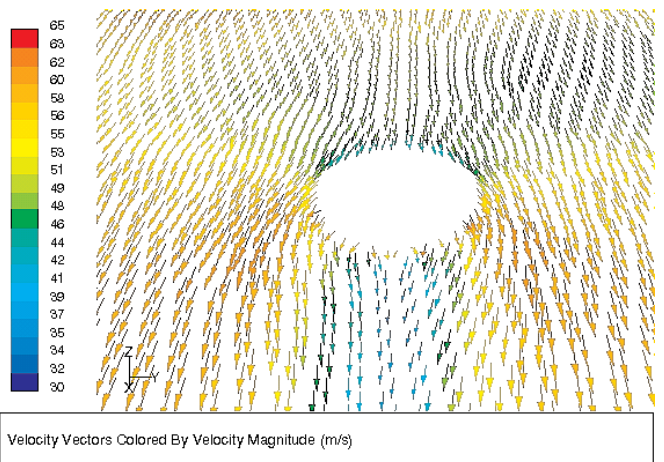

Figure 24. Velocity vectors on bodywork around the exhaust exit.

both cases, and also a considerable increment in aspiration in the no overlap configuration with respect to the 50% overlap.

In addition to the analysis of exhaust/bypass configuration, the 3-dimensional simulation was also employed to visualise the blockage caused on the free stream by the jet of exhaust gases. Although this is only a qualitative observation, the results from the oil flow experiments agree with the flow patterns seen on the bodywork surface in the CFD simulations. The blockage caused by the jet is repeated for every configuration tested, and due to the qualitative nature of the observation, significant differences were not observed. Figure 24 depicts the velocity direction vectors on the upper surface of the radiator pod. Because the mixing between the free stream and the exhaust jet does not take place instantaneously, the free stream air is forced around the exiting jet. Therefore, it follows that the exhaust jet causes the same blockage effect as a rigid body until complete mixing of the free stream and the jet is reached or the free stream has surrounded the jet completely.

Nevertheless, the resolution of the k-ε turbulence model, which can predict the counter rotating vortex structure, but not the horseshoe vortices, did not accurately capture the features of the wall boundary layer generated in the wake of the jet. This can justify the differences seen in the wake of the jet using the oil flow technique and the 3-dimensional simulations.

5.0 CONCLUSIONS

The possible shortcomings of the exhaust flow in a Formula One type of racing car have been studied. In terms of rear wing interference, it has been shown that the extra flow coming from the exhaust increases the aerodynamic lift of the aerofoil element. The possibility of increasing the down force of a Formula One car without increasing the drag of the vehicle is an area of significant interest, as maximum straight line and cornering speeds can be achieved. Nevertheless, this study has assumed and employed same temperature and very similar densities for all gases involved. It is reasonable to believe that an increment in temperature of the exhaust gases would enhance the discussed effects even further. It is conjectured that a heated exhaust stream would expand very rapidly once expelled into the atmosphere. As a result, the surface of the aerofoil being affected by the exhaust flow would be larger, compared with the case of a cold exhaust jet. Because the net force acting on the aerofoil can be defined as the average of the local forces, and the down force would be locally enhanced by a heated exhaust jet, we could conclude that a heated exhaust jet would increase the net down force acting on the wing element. However, further experimental and computational studies are required to support the above statements. The effects of the expulsion of the exhaust gases towards the lower surface of the rear wing element of the car at different ground-to-aerofoil heights and incidences on the drag and pitching moment coefficients will be addressed in a separate paper.

The oil flow technique revealed an interesting picture of the phenomena around the exhaust exit and depicted the solid-like behaviour of the exhaust jet, which would result in an increased drag of the vehicle.

The results from the computational study showed the optimum diameter ratio and overlap configuration to maximise aspiration through the bypass. The set of results obtained from both the 2 and 3 dimensional studies showed that, even though the k-ε is unable to predict the secondary coherent structures in the JICF concept, the major effects, such as the stream flow deflection[10,12,15], the boundary-layer vortex lift[13] and the bending over of the jet[16] can be predicted. In addition, the shape of the jet exit in the leeward side also plays an important role in the magnitude of the secondary coherent structures. The Coanda surface, exposed when the exhaust pipe is shortened, diminishes significantly the reversed flow area found in the wake of the jet with the full-length exhaust pipe.

REFERENCES

1. HOLMAN, J.P. *Heat Transfer*, 8th edition, McGraw-Hill, USA, 1997, Chaps 1,5.
2. MI, J. and NATHAN, G.J. Effect of small vortex-generators on scalar mixing in the developing region of a turbulent jet, *Int J Heat and Mass Transfer*, 1999, **42**, pp 3919-3926.
3. RAHAI, H.R. and WONG, T.W. Flow field characteristics of turbulent jets from round tubes with coil inserts, *Applied Thermal Engineering*, 2002, **22**, pp 1037-1045.
4. HILGERS, A. and BOERSMA, B.J. Optimization of turbulent jet mixing, *Fluid Dynamics Research*, 2001, **29**, pp 345-368.
5. RAHAI, H.R., VU, H.T. and SHOJAEE FARD, M.H. Mixing enhancement using a coil insert, *Applied Thermal Engineering*, 2001, **21**, pp 303-309.
6. REYNIER, P. and MINH, H.H. Numerical prediction of unsteady compressible coaxial jets, *Computers and Fluids*, 1998, **27**, (2), pp 239-254.
7. RIFFAT, S.B., GAN, G. AND SMITH, S. Computational fluid dynamics applied to ejector heat pumps, *Applied Thermal Engrg*, 1996, **16**, (4), pp 291-297.
8. HUANG, B.J., CHANG, J.M., WANG, C.P. and PETRENKO, V.A. A 1-D analysis of ejector performance, *Int J Refrigeration*, 1999, **22**, pp 354-364
9. MARGASON, R.J. Fifty years of cross flow research, Computational and Experimental Assessments of Jets in Cross Flow, number CP 534, 1993, AGARD.
10. HUSSAIN, A.K.M.F. Coherent structures and turbulence, *J Fluid Mechanics*, 1996, 306, pp 111-144.
11. RIVERO, A., FERRE, J.A. and GIRALT, F. Organized motions in a jet in cross flow, *J Fluid Mechanics*, 2001, **444**, pp 111-149.
12. RUDMAN, M. Simulation of the near field of a jet in a cross flow, *Experimental, Thermal and fluid Science*, 1996, **12**, pp 134-141.
13. DEMUREN, A.O. Numerical calculations of steady three dimensional turbulent jets in cross flow, *Computer Methods in Applied Mechanics and Engineering*, 1983, **37**, pp 309-328.
14. FRIC, T.F. and ROSHKO, A. Vortical structure in the wake of a transverse jet, *J Fluid Mechanics*, 1994, **279**, pp 1-47
15. ANDREOPOULOS, J. and RODI, W. Experimental investigation of jets in a crossflow, *J Fluid Mechanics*, 1984, **138**, pp 92-127
16. GOGINENI, S., GOSS, L. and ROQUEMORE, M, Manipulation of a jet in cross flow, *Experimental Thermal and Fluid Science*, **16**, 1998, pp 209-219
17. MORTON, B.R. and IBBETSON, A. Jets deflected in a crossflow, Experimental, *Thermal and Fluid Science*, 1996, **12**, pp 112-133
18. KONTIS, K. and STOLLERY, J.L. Control effectiveness of a jet-slender body combination at hypersonic speeds, *J Spacecraft and Rockets*, 1997, **34**, (6), pp 762-768
19. http://www.fia.com/sport/Regulations/f1regs.html
20. LOPEZ-PARRA, F. Vehicle Exhaust and Rear Wing Aerodynamic Interference and Optimisation Studies at Subsonic Speeds, MSc Dissertation, Mechanical, Aerospace and Manufacturing Engineering Department, UMIST, Manchester, UK, 2002.
21. LADA, C., AMIR, M., WONG, C. and KONTIS, K. Effect of dimples on glancing shock wave turbulent boundary-layer interactions, AIAA 2004-1058, 2004.
22. LAUNDER B.E., AND SPALDING, D.B. *Lectures in Mathematical Models of Turbulence*, Academic Press, London, England, UK, 1972.
23. LESCHZINER, M.A. AND DRIKAKIS, D. Turbulence modelling and turbulent-flow computation in aeronautics, *Aeronaut J*, 2002, **106**, (1061), pp 349-384.
24. BOSNIAKOV, S. Experience in integrating CFD to the technology of testing models in wind tunnels, *Progress in Aerospace Sciences*, 1998, **34**, pp 391-422.
25. DRIKAKIS, D. and GOLDBERG, U. Wall-distance-free turbulence models applied to incompressible flows, *Int J of Comput Fluid Dyn*, 1998, **10**, pp 241-253.
26. YAKHOT, V. and ORSZAG, S.A. Renormalization group analysis of turbulence: I. Basic Theory, *J Scientific Computing*, 1986, **1**, (1), pp 1-51.
27. SHIH, T.H., LIOU, W.W., SHABBIR, A., YANG, Z., and ZHU. J. A New k-ε eddy-viscosity model for high Reynolds number turbulent flows-model development and validation, *Computers Fluids*, 1995, **24**, (3), pp 227-238.